

Ionic exclusion phase transition in neutral and weakly charged cylindrical nanopores

Sahin Buyukdagli*, Manoel Manghi†, and John Palmeri‡

*Université de Toulouse; UPS;
Laboratoire de Physique Théorique (IRSAMC); F-31062 Toulouse, France and
CNRS; LPT (IRSAMC); F-31062 Toulouse, France*

(Dated: May 15, 2022)

A field theoretic variational approach is introduced to study ion penetration into water-filled cylindrical nanopores in equilibrium with a bulk reservoir. It is shown that (i) an ion located in a neutral pore undergoes two opposing mechanisms: the deformation of its surrounding ionic cloud of opposite charge, with respect to the reservoir, which increases the surface tension and tends to exclude ions from the pore, and (ii) the attractive contribution to the ion self-energy of the repulsive image forces associated with the dielectric jump between the solvent and the pore wall, which becomes more and more screened when ions enter the pore. For pore radii around 1 nm and bulk concentrations lower than 0.2 mol/L, this mechanism leads to a first-order phase transition, similar to capillary “evaporation”, from an ionic-penetration state to an ionic-exclusion state. The discontinuous phase transition survives within the biological concentration range (~ 0.15 mol/L) for small enough membrane dielectric permittivities ($\epsilon_m < 5$). In the case of a weakly charged pore, counterion penetration exhibits a non-monotonic behaviour and is characterized by two regimes: at low reservoir concentration or small pore radii, coions are excluded and the energy barrier for counterions is reduced but image forces remain strong enough, so that the counterion partition coefficient in the pore decreases with increasing reservoir concentration up to a characteristic value; for larger reservoir concentrations, image forces are screened and the partition coefficient of counterions increases with the reservoir electrolyte concentration, as in the neutral case. Large surface charge densities ($> 2 \times 10^{-3}$ e/nm²) suppress the discontinuous transition by reducing the energy barrier for ion penetration and shifting the critical point towards very small pore sizes and molar reservoir concentrations. Our variational method is compared to a previous self-consistent approach and yields important quantitative corrections. The role of the curvature of dielectric interfaces is highlighted by comparing ionic penetration into slit and cylindrical pores. Finally, a charge regulation model is introduced in order to explain the effect of pH on ionic exclusion.

PACS numbers: 03.50.De, 87.16.D-, 68.15.+e

I. INTRODUCTION

Electrostatic forces induced by macroscopic dielectric bodies immersed in water regulate important phenomena such as the stability of colloidal suspensions [1], membrane assemblies [2], and ion selectivity by synthetic membranes [3] as well as in biological nanopores [4]. The image forces induced by the dielectric permittivity jump between dielectric bodies and the solvent surrounding them play a central role in these phenomena. Indeed, the equilibrium of similarly charged objects in a solvent is driven by the competition between the repulsive electrostatic interaction of their charges and the attractive van der Waals forces that originate from their low dielectric permittivity. This picture, valid at low ionic concentrations, is also the basis of the DLVO theory [5]. A very similar competition is known to determine the permeability of biological channels that regulate ion exchange between the exterior and interior of cells. The strong dielectric discontinuity between the membrane (dielectric permittivity $\epsilon_m \simeq 2$) and the water-filled channel

($\epsilon_w \simeq 78$) is at the origin of the high potential barrier for ion penetration into the pore. In 1969, Parsegian found that the energetic cost to move an ion from the bulk reservoir into a cylindrical pore of infinite length and radius $a = 0.2$ nm is approximately $16 k_B T$ [6]. This result clearly suggests that at room temperature, any biological pore would be totally impermeable to ions. From the numerical solution of the Debye-Hückel (DH) equation, it was later shown that the consideration of the finite length of the channel reduces this barrier up to $6 k_B T$ [7]. Levin [8] recently proposed an approximative, but reasonably accurate, analytical solution of the DH equation for a finite length cylinder. He also showed that the introduction of surface charges can further reduce this energy barrier by attracting counterions electrostatically. These theoretical considerations are mainly based on the Debye-Hückel theory which is known to underestimate ionic correlations by handling them at the linear level. Hence, it becomes imperative to develop analytical or numerical tools valid over a larger parameter range.

In the case of confined geometries characterized by a dielectric discontinuity, the existence of an infinite number of image charges for each ion does not allow for a reliable numerical investigation, such as MC simulations [9]. Differential equations for electrostatic potentials, that partially take into account ionic correlations

*Email: buyuk@irsamc.ups-tlse.fr

†Email: manghi@irsamc.ups-tlse.fr

‡Email: john.palmeri@irsamc.ups-tlse.fr

at a non-linear level (i.e. beyond the DH theory) were derived by Netz and Orland [10] within a field-theoretic variational formalism. These variational equations are too complicated to be solved analytically or even numerically [10]. A tractable variational method for neutral single and double planar interface systems was proposed in Ref. [11]. Because of the piecewise inverse variational screening length introduced in this method, the numerical minimization procedure still remains complicated and the approach does not allow one to handle the case of charged planar and neutral cylindrical interfaces. In this article, we propose a simpler variational method to study ion penetration into cylindrical nanopores within the grand canonical ensemble. The approach is based on a generalized Onsager-Samaras approximation [12] which assumes an electrostatic kernel with a uniform variational inverse screening length κ_v and a constant variational Donnan potential ϕ_0 in the pore. The latter enforces electroneutrality in the pore for charged pores [13]. We show here that the extremization of the variational grand potential with respect to κ_v and ϕ_0 yields two coupled variational equations,

$$\begin{aligned} \kappa_v^2 &= \frac{4\pi\ell_B}{\left\langle \frac{\partial w(\mathbf{r}; \kappa_v)}{\partial \kappa_v} \right\rangle} \sum_i q_i^2 \rho_{b,i} \left\langle e^{-\Phi_i(\mathbf{r}; \kappa_v)} \frac{\partial w(\mathbf{r}; \kappa_v)}{\partial \kappa_v} \right\rangle (1) \\ \int_{S_p} d\mathbf{S} \sigma_s &= V_p \sum_i q_i \rho_{b,i} \left\langle e^{-\Phi_i(\mathbf{r}; \kappa_v)} \right\rangle, \quad (2) \end{aligned}$$

where we define the pore average as $\langle A(\mathbf{r}) \rangle \equiv \int_{V_p} \frac{d\mathbf{r}}{V_p} A(\mathbf{r})$, V_p (p for pore) stands for the volume occupied by the confined ions, S_p is the charged surface, σ_s is the uniform surface charge density, q_i denotes the ion valency, and $\rho_{b,i}$ is the reservoir density of each ionic species. We also define the potential of mean force (PMF)

$$\Phi_i(\mathbf{r}; \kappa_v) \equiv -\ln \frac{\rho_i(\mathbf{r})}{\rho_{b,i}} = \frac{q_i^2}{2} w(\mathbf{r}; \kappa_v) + q_i \phi_0 \quad (3)$$

which is the change in the excess electro-chemical potential when an ion is brought from the bulk inside the pore at position \mathbf{r} (in the following, all energies are rescaled by the thermal energy $k_B T = \beta^{-1}$). The quantity $w(r, \kappa_v)$ incorporates dielectric and electrostatic solvation forces (see Fig. 1) and thus depends in a complex manner on κ_v , and will be calculated in Section II. It is the κ_v dependence of w that couples ϕ_0 to κ_v , without which ϕ_0 is simply the Donnan potential. The ability of the present method to go beyond the mean-field and DH theories makes it a valuable tool for exploring the physics of charged biological systems (lipid membranes, water channels...) where image forces cannot be neglected. The variational scheme, which handles ionic correlations and image forces at a non-linear level, was recently applied to charged slit pores [13].

The variational equations obtained by Netz and Orland [10] are equivalent to the closure equations established in the context of nanofiltration theories (see [14]

and [15] for a review). The closure equations were solved for spherical pores within a self-consistent approximation by Dresner [16], who observed a discontinuous phase transition from a high to a low ionic penetration state for decreasing reservoir concentration. Although the spherical geometry adopted by Dresner significantly simplifies the technical difficulties, it remains a toy-model since in reality, ion-penetration is controlled by thin channels connecting the pore to the reservoir. The closure equations were later solved within the mid-point approximation by Yaroshchuk [15] for a cylindrical pore. The mid-point approximation is equivalent to replacing the potential of mean force in the exponential of Eqs. (1–2) by its value in the middle of the pore, which leads to an underestimation of repulsive image forces and solvation deficit effects. As will be shown below, this approximation can overestimate the partition coefficients of ions in the pore by up to a factor of three.

This paper is organized as follows. We introduce in Section II the general lines of the field-theoretic approach for charged dielectric bodies and derive the variational grand potential for a cylindrical pore. Section III deals with ion penetration into a neutral pore of radius a . A first-order ionic exclusion transition from an ionic-penetration state to an ionic-exclusion state is found for a specific range of parameter values. We draw the phase diagram in the (a, ρ_b) space. We then compare our results with the self-consistent approach within the mid-point approximation of Yaroshchuk [15]. In order to compare the ionic penetration into slit [13] and cylindrical pores, we also compute the electrostatic potential and the variational free energy for two neutral concentric cylinders and study the limit of large cylinder radii with fixed separation. In Section IV, we first investigate the effect of a non-zero fixed surface charge on ion partitioning and show that the transition survives for sufficiently weak surface charge density, but disappears above a critical value because of extra counterion penetration into the nanopore. Finally, we develop our approach for the case where the surface charge density is regulated by the pH (surface charge regulation mechanism) which occurs experimentally for nanotubes in PET membranes [17] where weak acid groups are located at the pore surface. The calculation of the Green's function for a cylindrical dielectric interface [18] is presented in Appendix A and for two concentric cylinders in Appendix B.

II. MODEL

In this section, we compute the variational grand potential of a symmetric electrolyte of dielectric permittivity ϵ_w (identical to the bulk value) confined in a cylinder of radius a and length L . The cylindrical pore traversing a membrane is depicted in Fig. 1. The membrane of dielectric permittivity ϵ_m is salt free (i.e. $\kappa = 0$) and the electrolyte is in contact with an external particle reservoir at the end boundaries of the cylinder. Hence the fugac-

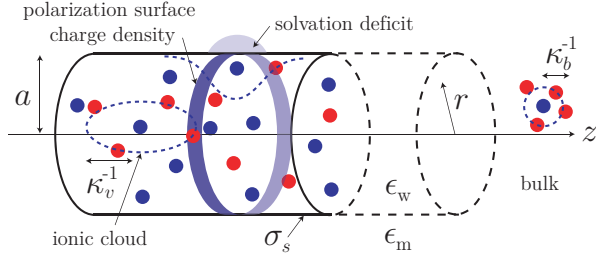


FIG. 1: Geometry for a cylindrical pore of infinite length and radius a . The ionic cloud is distorted due to the dielectric repulsion by the polarization surface charge density and the solvation deficit outside the pore.

ity of ions is $\lambda_i = e^{\mu_i}/\Lambda_i^3$, where $\Lambda_i = h/\sqrt{2\pi m_i k_B T}$ is the thermal De Broglie wavelength of an ion i and μ_i its chemical potential, and it is fixed inside the pore according to the chemical equilibrium condition, $\lambda_i = \lambda_{i,b}$.

The grand-canonical partition function of p species of interacting charges is

$$\mathcal{Q} = \prod_{i=1}^p \sum_{N_i=0}^{\infty} \frac{\lambda_i^{N_i}}{N_i!} \int \prod_{j=1}^{N_i} d\mathbf{r}_j e^{-(E_c - E_s)} \quad (4)$$

The electrostatic interaction in Eq. (4) is given by

$$E_c = \frac{1}{2} \int d\mathbf{r} d\mathbf{r}' \rho(\mathbf{r}) v_c(\mathbf{r}, \mathbf{r}') \rho(\mathbf{r}') \quad (5)$$

where the charge distribution, in units of the elementary charge e , is

$$\rho(\mathbf{r}) = \sum_{i=1}^p \sum_{j=1}^{N_i} q_i \delta(\mathbf{r} - \mathbf{r}_j) + \rho_s(\mathbf{r}), \quad (6)$$

and $\rho_s(\mathbf{r}) = \sigma_s \delta(|\mathbf{r}| - a)$ is the negative fixed charge distribution ($\sigma_s < 0$) at the surface of the cylinder. The electrostatic potential $v_c(\mathbf{r}, \mathbf{r}')$ is solution of

$$v_c^{-1}(\mathbf{r}, \mathbf{r}') = -\frac{1}{\beta e^2} \nabla [\epsilon(\mathbf{r}) \nabla \delta(\mathbf{r} - \mathbf{r}')] \quad (7)$$

where

$$\epsilon(\mathbf{r}) = \epsilon_m \Theta(|\mathbf{r}| - a) + \epsilon_w \Theta(a - |\mathbf{r}|) \quad (8)$$

is the dielectric permittivity (where $\Theta(x)$ is the Heaviside distribution). Furthermore, the bulk self-energy of

mobile ions that we subtract from the total electrostatic energy in Eq. (4) is

$$E_s = \frac{v_c^b(0)}{2} \sum_{i=1}^p N_i q_i^2. \quad (9)$$

The bare Coulomb potential in the bulk is $v_c^b(\mathbf{r}) = \ell_B/r$, where the Bjerrum length is defined as $\ell_B = e^2/(4\pi\epsilon_w k_B T) \simeq 0.7$ nm in water at $T = 300$ K. After performing a Hubbard-Stratonovitch transformation and summing over N_i in Eq. (4), the grand-canonical partition function becomes $\mathcal{Q} = \int \mathcal{D}\phi e^{-H[\phi]}/Z_c$, where the field-theoretic Hamiltonian is

$$H[\phi] = \int d\mathbf{r} \left[\frac{\epsilon(\mathbf{r})}{2\beta e^2} [\nabla\phi(\mathbf{r})]^2 - i\sigma(\mathbf{r})\phi(\mathbf{r}) - \sum_i \tilde{\lambda}_i e^{iq_i\phi(\mathbf{r})} \right] \quad (10)$$

where we have introduced the rescaled fugacities, $\tilde{\lambda}_i = \lambda_i e^{\frac{q_i^2}{2} v_c^b(0)}$. The electrostatic potential $\psi(\mathbf{r})$ is related to the fluctuating field $\phi(\mathbf{r})$ by $\psi(\mathbf{r}) = i\langle\phi(\mathbf{r})\rangle$. The factor Z_c in the partition function subtracts the non-screened van der Waals contribution. Since we are exclusively interested in the salt-dependent part of the grand potential, we keep Z_c in the functional integral. The variational method consists in extremizing, with respect to the variational parameters, the first-order cumulant $\Omega_v = \Omega_0 + \langle H - H_0 \rangle_0$ where the expectation values $\langle \dots \rangle_0$ are evaluated with the variational Gaussian Hamiltonian

$$H_0[\phi] = \frac{1}{2} \int_{\mathbf{r}, \mathbf{r}'} [\phi(\mathbf{r}) - i\phi_0(\mathbf{r})] v_0^{-1}(\mathbf{r}, \mathbf{r}') [\phi(\mathbf{r}') - i\phi_0(\mathbf{r}')] \quad (11)$$

and $\Omega_0 = -\frac{1}{2} \text{tr} \ln(v_0/v_c)$. The variational parameters are the Green's function $v_0(\mathbf{r}, \mathbf{r}')$ and the electrostatic potential $\phi_0(\mathbf{r})$. In the following, we consider the restricted case of a constant variational ‘‘Donnan’’ potential ϕ_0 and $v_0(\mathbf{r}, \mathbf{r}')$ a solution of the inhomogeneous Debye-Hückel equation

$$[-\nabla(\epsilon(\mathbf{r})\nabla) + \epsilon(\mathbf{r})\kappa^2(\mathbf{r})] v_0(\mathbf{r}, \mathbf{r}') = \beta e^2 \delta(\mathbf{r} - \mathbf{r}') \quad (12)$$

with a variational inverse screening length defined by

$$\kappa(\mathbf{r}) = \kappa_v \Theta(a - |\mathbf{r}|). \quad (13)$$

After evaluating the functional integrals, the variational grand potential becomes

$$\frac{\Omega_v}{V_p} = -\sum_i \lambda_i \left\langle \exp \left[\frac{q_i^2}{2} (\kappa_v \ell_B - \delta v_0(\mathbf{r}, \mathbf{r}; \kappa_v)) - q_i \phi_0 \right] \right\rangle + \frac{\kappa_v^3}{24\pi} + \frac{\kappa_v^2}{8\pi\ell_B} \int_0^1 d\xi \left\langle \delta v_0(\mathbf{r}, \mathbf{r}; \kappa_v \sqrt{\xi}) - \delta v_0(\mathbf{r}, \mathbf{r}; \kappa_v) \right\rangle + \frac{2}{a} \sigma_s \phi_0 \quad (14)$$

where $V_p = \pi a^2 L$ and $\delta v_0(\mathbf{r}, \mathbf{r}; \kappa_v)$ (see Fig. 2) is the correction due to the presence of the nanopore to the variational Green function:

$$v_0(\mathbf{r}, \mathbf{r}'; \kappa_v) = \ell_B \frac{e^{-\kappa_v |\mathbf{r} - \mathbf{r}'|}}{|\mathbf{r} - \mathbf{r}'|} + \delta v_0(\mathbf{r}, \mathbf{r}'; \kappa_v) \quad (15)$$

evaluated at $\mathbf{r}' = \mathbf{r}$ [see Eq. (A9)], and is thus defined as

$$\delta v_0(\mathbf{r}, \mathbf{r}; \kappa_v) = \frac{4\ell_B}{\pi} \int_0^\infty dk \sum'_{m \geq 0} F_m(k; \kappa_v) I_m^2(\mathcal{K}|\mathbf{r}|) \quad (16)$$

where we note $\mathcal{K}^2 = k^2 + \kappa_v^2$ and the prime on the summation sign means that the term $m = 0$ is multiplied by $1/2$. The function F_m is a combination of modified

Bessel functions I_m and K_m and is given in Eq. (A10). Note that we have $F_m \rightarrow 0$ for $a \rightarrow \infty$ and thus $\delta v_0 \rightarrow 0$.

To find the physical meaning of the various contributions in Eq. (14), it is interesting to rewrite it in two ways. The classical thermodynamic equality in presence of surface effects, $\Omega_v = -pV_p + \gamma S_p$ with $S_p = 2\pi aL$, allows us to separate the volumic bulk contribution, the pressure, which is independent of a (or S_p)

$$p(\kappa_v) = \sum_i \lambda_i \exp\left(\frac{q_i^2 \kappa_v \ell_B}{2}\right) - \frac{\kappa_v^3}{24\pi} \quad (17)$$

and the surface tension, $\gamma = (\Omega_v + pV_p)/S_p$,

$$\gamma = -\frac{a}{2} \sum_i \lambda_i e^{q_i^2 \kappa_v \ell_B / 2} \left\langle e^{-q_i^2 \delta v_0(\mathbf{r}, \mathbf{r}; \kappa_v) / 2 - q_i \phi_0} - 1 \right\rangle + \frac{a\kappa_v^2}{16\pi\ell_B} \int_0^1 d\xi \left\langle \delta v_0(\mathbf{r}, \mathbf{r}; \kappa_v \sqrt{\xi}) - \delta v_0(\mathbf{r}, \mathbf{r}; \kappa_v) \right\rangle + \sigma_s \phi_0 \quad (18)$$

which is a function of nanopore characteristics (σ_s , a and ϵ_m *via* δv_0), and vanishes for $a \rightarrow \infty$. By maximizing the variational pressure in Eq. (17), we find the inverse screening length in the bulk, κ_b , given by the following implicit equation as a function of the fugacities λ_i :

$$\kappa_b^2 = 4\pi\ell_B \sum_i q_i^2 \lambda_i \exp\left(\frac{q_i^2 \kappa_b \ell_B}{2}\right). \quad (19)$$

Note that Eq. (19) leads to instabilities for large values of λ_i if hard-core repulsion is not included [19]. Moreover, Eq. (19) has no solution for large fugacities such that $q_i^2 \kappa_b(\lambda) \ell_B > 4$. For low fugacities, Eq. (19) yields the Debye-Hückel Limiting Law (DHLL). Indeed, the bulk density is computed through

$$\rho_{i,b}(\lambda) = \lambda_i \frac{\partial p}{\partial \lambda_i} = \lambda_i e^{\frac{q_i^2}{2} \kappa_b \ell_B} \quad (20)$$

which allows to rewrite Eq. (19) as

$$\kappa_b^2 = 4\pi\ell_B \sum_i q_i^2 \rho_{i,b}(\lambda). \quad (21)$$

In the following, we will keep ρ_b in the equations by replacing $\lambda e^{\frac{q_i^2}{2} \kappa_b \ell_B}$ by ρ_b in Eq. (14). Note that to get ρ_b , we calculate it from λ , which is fixed in the grand canonical ensemble, using Eqs. (19)-(20). Solving Eq. (20) for μ_i leads to the DHLL canonical ensemble result:

$$\mu_i = \ln(\rho_{i,b} \Lambda_i^3) - \frac{q_i^2}{2} \kappa_b \ell_B. \quad (22)$$

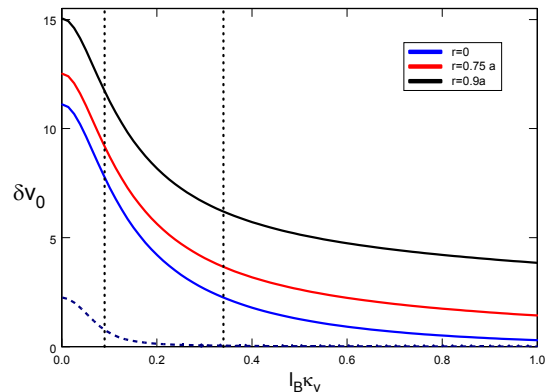


FIG. 2: Variation of δv_0 given in Eq. (16) with κ_v for three values of $r = 0, 0.75$, and $0.9a$ (solid lines from bottom to top) and $\epsilon_m = 2$, $\epsilon_w = 78$, and $a = 0.84$ nm. The dotted line corresponds to ϕ_0 for $|\sigma_s| = 5.4 \times 10^{-4}$ nm⁻² and $\rho_b = 0.1812$ mol/L. The left and right reference lines mark the solutions of κ_v just below and above the transition point, respectively.

The second way to interpret Eq. (14) is by remarking that the first term of the rhs looks like the pressure of an ideal gas of ions “dressed” by their surrounding cloud, in a self-consistent or “external” field, $\frac{q_i^2}{2}(-\kappa_v \ell_B + \delta v_0(\mathbf{r}, \mathbf{r}; \kappa_v)) + q_i \phi_0$. It favors high κ_v . The second and third terms are the correlation contribution, or the charging energy needed to create dressed ions [20], modified by the nanopore. They come from “attractive” correlations between ions and their surrounding ionic cloud of opposite charge [20]. They favor low κ_v since Ω_v

increases when κ_v increases even if $\delta v_0(\kappa_v)$ is a decreasing function of κ_v (see Fig 2). The second term is minus the DH pressure of a hypothetical bulk of inverse screening length κ_v and the third one is the surface tension due to the presence of the nanopore (dielectric exclusion and modified solvation effects). When κ_v is set arbitrarily to 0 (no screening, which corresponds to “phantom ions”), one ends up with a barometric law, i.e. a ideal gas in the external potential, $\frac{q_i^2}{2}\delta v_0(\mathbf{r}, \mathbf{r}; 0) + q_i\phi_0$, induced by the dielectric discontinuity at the pore surface. In summary, this system can be viewed as an ideal gas of dressed ions, whose accessible space is reduced by dielectric repulsion. Both the Boltzmann weight, which takes into account the feedback correlation associated with the fact that ions forming the surrounding cloud are themselves dressed ions, and the repulsive dielectric self-energy contribution are modified when the screening parameter, κ_v , varies.

The PMF, defined in Eq. (3), includes the potential $w(r)$ that incorporates the solvation and image-charge interactions

$$\begin{aligned} w(r) &= v_0(r, r) - v_c^b(0) + \kappa_b(\lambda)\ell_B \\ &= (\kappa_b - \kappa_v)\ell_B + \delta v_0(r, r; \kappa_v). \end{aligned} \quad (23)$$

where κ_b is defined in Eq. (19). The quantity $q_i^2 w(r)/2$ is the difference between the excess chemical potential of ion i located at distance r in the nanopore and the excess chemical potential of the same ion in the bulk [13]. It is a decreasing function of κ_v , since increasing κ_v increases the electrostatic solvation gain of the hypothetical bulk (usual DH excess chemical potential term in $-\kappa_v\ell_B$) and, $\delta v_0(\kappa_v)$ decreases very slowly for very low and large κ_v and abruptly at intermediate κ_v ($\kappa_v^{-1} \simeq 2a$ the pore diameter, see Fig. 2), since the direct dielectric exclusion begins to be screened.

By minimizing Eq. (14) with respect to κ_v , one exactly obtains Eq. (1) of the Introduction with $w(\mathbf{r}, \kappa_v)$ defined in Eq. (23). Note that for a bulk electrolyte ($a \rightarrow \infty$) treated variationally, Eq. (1) yields the Debye-Hückel relation Eq. (21) as long as the stability condition on fugacities λ_i , $q_i^2 \kappa_b \ell_B < 4$ ($\rho_b < 3$ mol/L for monovalent ions) discussed in [13] is satisfied. The drawback of working directly with Eq. (1) is that when it has three distinct solutions for κ_v , one cannot distinguish between stable, metastable and unstable solutions. For this reason, in the following, we will analyze the pore-electrolyte model within the free energy minimization procedure and use Eq. (1) exclusively to show the importance of quantitative errors induced by a previous self-consistent approach [15, 16].

Finally, ion concentrations in the pore are calculated using

$$\langle \rho_i(r) \rangle = -\lambda_i \frac{\partial(\Omega_v/V_p)}{\partial \lambda_i} \quad (24)$$

$$= \lambda_i e^{\frac{q_i^2}{2}\kappa_v\ell_B} \left\langle e^{-\frac{q_i^2}{2}\delta v_0(\mathbf{r}, \mathbf{r}; \kappa_v) - q_i\phi_0} \right\rangle. \quad (25)$$

We introduce the partition coefficients, which are measurable quantities, for instance in ion conductivity experiments, defined as

$$k_i \equiv \frac{\langle \rho_i(r) \rangle}{\rho_b} = \frac{2}{a^2} \int_0^a dr r e^{-\frac{q_i^2}{2}w(r) - q_i\phi_0}. \quad (26)$$

In the rest of the paper, we will consider a symmetric electrolyte, i.e. $q_+ = -q_- = q$. By differentiating the variational grand potential (14) with respect to ϕ_0 , one simply obtains the electroneutrality condition Eq. (2) which for a cylindrical nanopore is simply

$$\sigma_s = q\rho_b a \Gamma \sinh(q\phi_0) \quad (27)$$

where we have defined the coefficient

$$\Gamma \equiv \left\langle e^{-\frac{q^2}{2}w(r)} \right\rangle = 2 \int_0^1 dx x e^{-\frac{q^2}{2}w(xa)} \quad (28)$$

which accounts for solvation and image corrections to mean-field theory (corresponding to $\Gamma = 1$). By inverting Eq. (27) we find

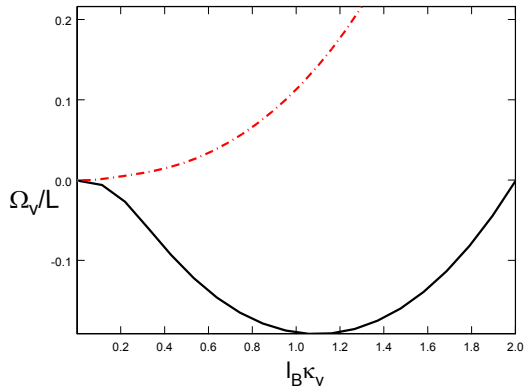
$$q\phi_0 = \ln \left[\frac{-\gamma + \sqrt{\gamma^2 + (q\Gamma)^2}}{q\Gamma} \right] \quad (29)$$

where we have defined $\gamma = |\sigma_s|/(\rho_b a) = X_m/(2\rho_b)$, $X_m = 2|\sigma_s|/a$ being the volume charge density of the pore. By injecting the solution Eq. (29) into the grand potential (14), we are left with a single variational parameter κ_v that will be varied in order to find the optimal solutions to the variational problem.

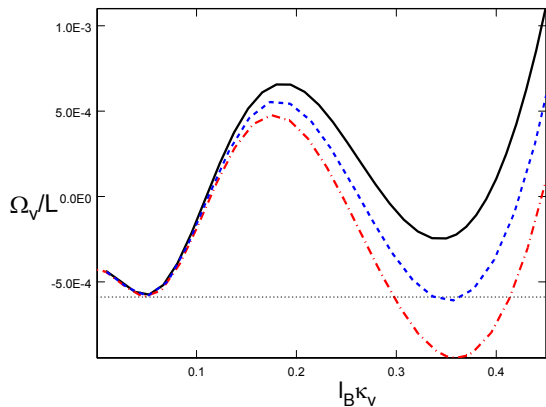
III. NEUTRAL PORE

In this section, we investigate the exclusion of ions from a neutral cylindrical pore. The electrolyte in the bulk reservoir is symmetric and composed of monovalent ions ($q = 1$). The vanishing surface charge, $\sigma_s = 0$, imposes $\phi_0 = 0$ through Eq. (27). In Fig. 3a and 3b are plotted the variational grand potential Ω_v vs the adimensional variational inverse screening length $\ell_B \kappa_v$ for pore radius $a = 0.84$ nm, $\epsilon_m = 2$ (the case for lipid membranes), and various bulk concentration ρ_b . Figure 3a shows that as one reduces the reservoir concentration from $\rho_b = 0.77$ mol/L to $\rho_b = 0.12$ mol/L, the minimum of the grand potential changes from $\ell_B \kappa_v^L \simeq 1.1$ ($\langle \rho \rangle = 0.2524$ mol/L) to $\ell_B \kappa_v^V = 0.037$ ($\langle \rho \rangle = 3 \times 10^{-4}$ mol/L). In other words, the pore evolves from an *ionic-penetration state* (L) to a quasi total *ionic-exclusion* one (V).

If one now slowly increases the bulk concentration from $\rho_b = 0.12$ mol/L to, for instance, $\rho_b = 0.181$ mol/L, one notices the apparition of a second minimum at moderate $\ell_B \kappa_v \simeq 0.34$, shown in Fig. 3b, which corresponds to a significant ion concentration in the pore, $\rho_L = 29$ mmol/L. One sees that this minimum is



(a)



(b)

FIG. 3: Variational grand potential vs κ_v for $\epsilon_m = 2$, $\epsilon_w = 78$ and $a = 0.84$ nm. From bottom to top, bulk concentrations are (a) $\rho_b = 0.777$ and 0.123 mol/L, and (b) $\rho_b = 0.181$, 0.183 , and 0.185 mol/L.

metastable and the stable solution is the one corresponding to the ionic-exclusion state with $\rho_b = 0.44$ mmol/L. If we keep increasing the reservoir concentration up to $\rho_b^c = 0.1832$ mol/L, the values of both minima become equal, which indicates a *phase coexistence*: indeed, the equality of the two values of the grand potential, $\Omega_v(\kappa_v^V) = \Omega_v(\kappa_v^L)$, indicates mechanical equilibrium between both states. Finally, as ρ_b is increased further to $\rho_b = 0.185$ mol/L, the ionic-exclusion state becomes metastable and the pore becomes penetrable to ions.

This behaviour is the signature of a *first-order phase transition* over a certain parameter range for cylindrical nanopores. Note that such a transition does not appear to take place in slit-like pores [13] although a continuous crossover from the presence to the absence of ions has already been observed for slit-like pores within a self-consistent calculation in Refs. [15, 16] and within the variational approach in Ref. [11, 13] (see Figs. 7-9).

This discontinuous transition is characterized in Fig. 4 where we display for $\epsilon_m = 2$ the partition coefficients, given by Eq. (26), corresponding to the *stable state* of the variational grand potential, as a function of the reservoir

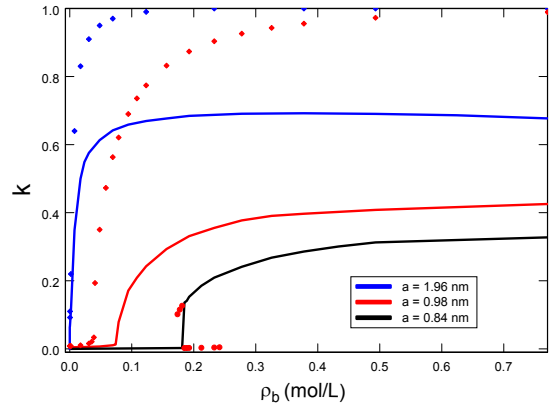


FIG. 4: Partition coefficients vs ρ_b for $\epsilon_m = 2$, $\epsilon_w = 78$, and pore radii $a = 1.96$, 0.98 and 0.84 nm (solid lines, from top to bottom). The (red) circles display the metastable solutions, thus defining the coexistence window. Blue and red diamonds correspond to the solution of the self-consistent mid-point approximation Eq. (31) for $a = 1.96$, and 0.98 nm.

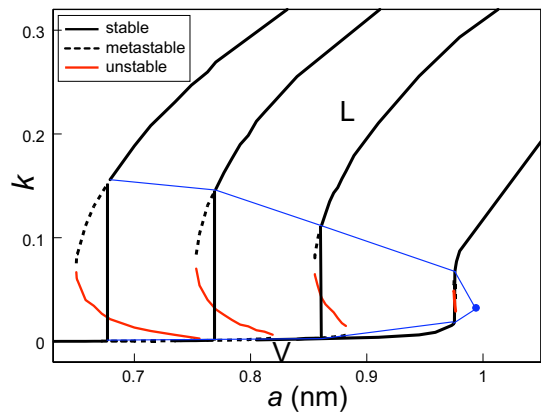


FIG. 5: Partition coefficient $k = \langle \rho \rangle / \rho_b$ inside a *neutral* nanopore ($q = 1$, $\epsilon_m = 2$, $\epsilon_w = 78$) vs the pore radius a for, from left to right, $\rho_b = 0.7, 0.3, 0.156, 0.08$ mol/L (“isobars”). Dotted (grey/red) lines show metastable (unstable) branches, light grey/blue lines (guide for the eye) are the “boiling point” curve (bottom) and the “dew point” curve (top) and the dot is the critical point, $\rho_b^* = 0.075$ mol/L, $a^* = 0.987$ nm.

concentration ρ_b for three different radii. At large pore size $a = 1.96$ nm, the discontinuous jump is absent and the transition to the ionic-exclusion state is a continuous crossover. At a critical pore radius $a^* = 0.987$ nm, a continuous phase transition occurs, where a single minimum exists for Ω_v which evolves towards lower ion concentrations in the pore with decreasing reservoir concentration in a fast but continuous way (data not shown). For $a = 0.98$ nm ($a < a^*$), the discontinuous jump at the coexistence bulk concentration exists, but with a very small jump for the partition coefficient.

This is illustrated in Fig. 5 where is shown the par-

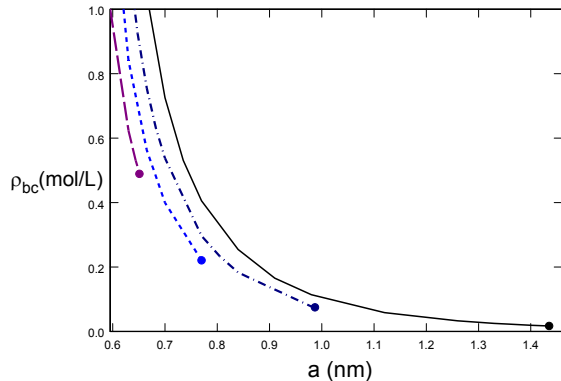


FIG. 6: Phase diagram characterizing the discontinuous phase transition for neutral pores ($\epsilon_w = 78$ and $\epsilon_2 = 1, 2, 3, 4$, from right to left). The critical line separates the ionic-penetration L state (area above the curve) from the ionic-exclusion V state (area below the curve) and ends at the critical point (dot) where the transition becomes continuous and then disappears.

tion coefficient k versus the pore size for various ρ_b . The metastable and unstable branches are shown in blue and the critical point, where the transition becomes second order, is for $\rho_b^* = 0.075$ mol/L, $a^* = 0.987$ nm. One notices the resemblance with the liquid-vapor (L-V) phase transition in bulk fluids, showing the “boiling point” curve and the “dew point” curve. Indeed, by interchanging the pore size, the partition coefficient of ions in the pore and the reservoir electrolyte density respectively with the temperature, the density and the pressure of a bulk liquid, one notices that the first-order exclusion transition becomes analogous to a bulk liquid-vapor (L-V) transition.

To determine the parameter regime in which the discontinuous transition takes place, the phase diagram is shown in Fig. 6 for $\epsilon_w = 78$ and $\epsilon_m = 1$ to $\epsilon_m = 4$, where the lines correspond to the reservoir concentration at the coexistence point versus the pore radius, $\rho_b^c(a)$. Each curve corresponds to the coexistence line separating the ionic-penetration state, L, (the area above the curve) from ionic-exclusion state, V (below the curve). The lines end at the ϵ_m dependent critical point (a^*, ρ_b^*), marked by a dot beyond which the transition disappears. One first notices that the parameter regime where the phase separation is observable is considerably reduced when increasing ϵ_m . The critical end-point evolves towards smaller pore sizes and higher reservoir densities. For $\epsilon_w = 78$ and ϵ_m from 1 to 4 (the curves in Fig. 6), the critical pore size is $a^* = 1.44, 0.99, 0.77$ and 0.65 nm while the critical reservoir concentration is $\rho_b^* = 17, 75, 221$ and 489 mmol/L, respectively. Higher values of ϵ_m are not considered in this work since the coexistence line would correspond in this case to very high bulk densities and extremely small pore sizes, where hard-core effects, which are not yet incorporated in our model, become

non-negligible.

It is clear from Fig. 6 that the membrane dielectric permittivity ϵ_m , and thus dielectric repulsive forces, plays a central role in the mechanism of the phase transition. Moreover, it is known that the geometry influences the intensity of this dielectric repulsion. In order to investigate curvature effects on the ionic exclusion mechanism, we compare in Fig. 7 the ion partition coefficients in cylindrical (continuous lines) and slit pores (dashed lines). It is seen that as long as one is far from the transition point, the ion density in a cylindrical pore of radius a (diameter $2a$) is very close to that in a slit pore of thickness $d = a$ and the difference becomes smaller with increasing pore size a and/or reservoir concentration ρ_b . In order to explain this equivalence, we computed within the variational approach the partition coefficient of ions confined between neutral concentric cylinders of radius a_1 and $a_2 > a_1$ (technical details are given in Appendix B). The result is illustrated in Fig. 7 for $\rho_b = 0.075$ mol/L and $\rho_b = 0.123$ mol/L by two sets of points computed at a fixed distance between the cylinders, i.e. $\delta = a_2 - a_1 = 0.98$ nm. The inner radius a_1 is varied from top to bottom between 0.7 and 0 nm. At $\rho_b = 0.123$ mol/L and $a_1 = 0.7$ nm (the highest point), it is shown that the curvature of both cylinders is so weak that the ion concentration between the concentric cylinders is the same as that in the slit pore with $d = \delta$, as expected. By decreasing gradually a_1 from this value to 0 , one naturally recovers the ionic partition function in a cylindrical pore. For $\rho_b = 0.075$ mol/L, the interpolation between the slit pore and the cylindrical pore occurs in a similar way, except that since the pore radius $a = \delta$ corresponds to the exclusion state, the partition coefficient drops to nearly 0 between $a_1 = 0.119$ nm (the sixth point from the top) and $a_1 = 0.112$ nm (the seventh point from the top). Hence, we conclude that the equivalence in ionic penetration for cylindrical pores of radius a and slit pores of thickness $d = a$ is simply the reminiscence of the concentric cylindrical case where for large values of the inner and outer radii (and the weak curvature of the dielectric interfaces), the system qualitatively behaves as a slit pore.

The existence of stronger dielectric forces in a cylindrical pore with respect to a slit one can thus be explained in terms of curvature. It is well-known that if the ion sees a dielectric interface with a positive curvature, i.e. if the interface is curved towards the ion, the experienced repulsion will be stronger than in the case where it would be placed face to a planar interface [21]. On the contrary, if the ion is close to a negatively-curved interface, such as a protein or DNA, the dielectric exclusion will be weaker compared to a planar interface. This is the reason why the cavity correction factor of proteins measured in experiments is below one [22]. Therefore, the positive curvature of the pore is the essential ingredient for the existence of a discontinuous phase transition.

At the first-order variational level [see Eq. (14)], ion penetration is essentially driven by two op-

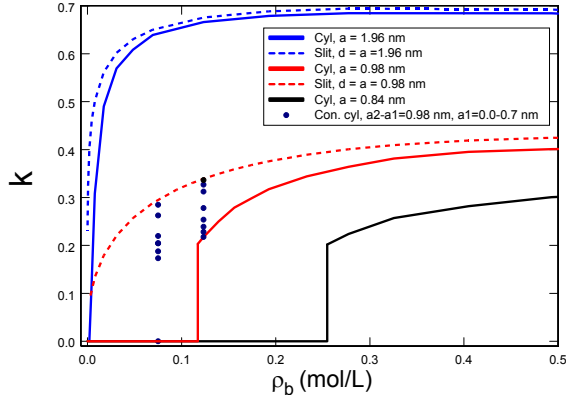


FIG. 7: Same figure as Fig. 4 for $\epsilon_m = 1$. Solid lines correspond to a cylindrical pore and dotted lines to a slit pore whose width is $d = a$. Solid circles correspond to the partition coefficient of an electrolyte confined between two concentric cylinders of a fixed width $\delta = a_2 - a_1 = a$ and show the crossover from a slit to cylindrical pore when a_1 varies from ∞ to 0.

posing mechanisms which contribute to the surface tension γ , given in Eq. (18). On the one hand, due to “attractive” correlations between ions and their oppositely charged surrounding cloud, the $\kappa_v^2 \int d\xi \langle \delta v_0(\mathbf{r}, \mathbf{r}, \kappa_v \sqrt{\xi}) - \delta v_0(\mathbf{r}, \mathbf{r}, \kappa_v) \rangle$ term of the surface tension increases with increasing κ_v , which is sensitive to the variations of κ_v since increasing κ_v leads to the screening of δv_0 (see Fig. 2). This cost in surface tension is thus associated with the deformation of the ionic cloud of each ion, due to dielectric repulsion.

On the other hand, the presence of the pore walls decreases the volume accessible to ions compared to an hypothetical bulk, and contributes negatively to the surface tension (this contribution vanishes for $\kappa_v = 0$). When κ_v increases, the dielectric repulsion becomes screened and the number of ions penetrating the nanopore increases (due to the Boltzmann law), which decreases the surface tension. Indeed, the Gibbs adsorption equation at constant temperature is

$$d\gamma = -(\langle \rho \rangle - \rho_b) d\mu. \quad (30)$$

By increasing κ_v , Eq. (23) leads to $d\mu < 0$, and since there is desorption in the nanopore ($\langle \rho \rangle < \rho_b$), $d\gamma < 0$: this is favorable to the system.

Note that this liquid-vapor phase transition exists for bulk electrolytes but at very low temperature ($T \approx 100$ K) for usual salts [23–26]. The critical temperature T^* is thus shifted towards room temperature in pores of nanometer radius due to surface effects. Indeed, essentially due to dielectric repulsion, the low dielectric surface favors the vapor phase and thus shifts the first-order transition. We thus call this phenomenon *capillary evaporation*, just as for water in capillaries which undergoes

condensation for hydrophilic surfaces [27–30] and evaporation for hydrophobic ones [31, 32].

The possibility for the existence of a first-order phase transition for electrolytes confined in *spherical* pores was first pointed-out by Dresner [16]. He used an approximate Green’s function, which is exact at the center of a spherical pore, and a self-consistent approach to show that the first-order phase transition survives as long as $\epsilon_m \ll \epsilon_w$. However, because of the numerous approximations introduced in his work, Dresner [16] recognized that the quantitative predictions of this approach were not reliable. Yaroschuk [15] later performed a similar self-consistent calculation using the correct Green’s function at the center of a *cylindrical* pore and showed that the discontinuous phase transition to an ionic-exclusion state also comes out from this more rigorous approach. However, he also argued that this phase transition is unphysical because it comes from the use of the DH equation, which ignores non-linear effects. By introducing a non-linear DH equation (by analogy with the non-linear PB equation), he argued that the first-order phase transition disappears. However, this PB-like generalization of the DH equation is incorrect as already argued by Onsager in the 30s [33]. It is indeed known that in the most general form of the first-order variational theory, whose order also corresponds to the perturbative order of the self-consistent approach used by Dresner [16] and Yaroschuk in [15], the corrective term taking into account non-linear effects is $e^{-q^2 v_0(\mathbf{r}, \mathbf{r})/2}$, which multiplies the salt term of the usual DH equation [10, 15]. Hence, we argue that, within the confined electrolyte model presented in this work, the existence of a first-order phase transition is physical.

We finally analyze Yaroschuk’s self-consistent (SC) approach. It consists in finding self-consistently the screening parameter κ by defining κ^2 as the average value of $\kappa_b^2 e^{-\Phi(\mathbf{r}, \kappa)}$ in the pore [15]. To pursue, he replaced the PMF within the integral by its value on the pore-axis, which in turn causes an underestimation of repulsive dielectric forces that become significantly stronger close to the pore wall. He obtained what we call the “mid-point approximation” for κ :

$$\kappa^2 = \kappa_b^2 e^{-\frac{q^2}{2} w(0, \kappa)} \quad (31)$$

where κ_b is defined in Eq. (21). The partition coefficients in a neutral pore obtained from the numerical solution of Eq. (31) are compared in Fig. 4 with the prediction of our variational approach for $a = 1.96$ and 0.98 nm. It is clearly seen that the mid-point approximation overestimates ionic penetration into the pore, which is due to the underestimation of dielectric forces, as stressed above. This point was also noticed for slit-pores in our previous work [13]. As one sees in Fig. 4, the error induced by Yaroschuk’s approach increases with decreasing pore size, which originates from the amplification of image forces when one decreases the pore radius. One notices that for $a = 0.98$ nm the partition coefficients as

well as the position of the transition point predicted by the mid-point approximation can deviate from the prediction of our variational method by 200–300 %.

IV. CHARGED PORE

A. Fixed surface charge

In this part, we investigate ion penetration into a cylindrical nanopore of non-zero fixed surface charge density, $\sigma_s < 0$. We first note that the electroneutrality condition Eq. (27) can be written, using Eq. (26), as

$$k_+ - k_- = \frac{2|\sigma_s|}{q\rho_b a} = \frac{X_m}{q\rho_b}. \quad (32)$$

We introduce the *good coion exclusion* (GCE) limit which corresponds to the counterion-only case in the nanopore. In the case of slit pores, it was shown that the *charge repulsion* GCE limit is reached for small pore sizes, strong surface charge, and low bulk concentrations even without any dielectric effects [13] ($\Gamma \approx 1$, $2|\sigma_s|/(q\rho_b a) \gg 1$) and associated with the electric repulsion of coions. In the case of cylindrical nanopores, a second *dielectric repulsion* GCE limit exists for low $|\sigma_s|$ as soon as $\Gamma \ll 2|\sigma_s|/(q\rho_b a)$. The partition coefficients of ions in the cylindrical pore become

$$k_+ \simeq \frac{2|\sigma_s|}{q\rho_b a} \quad \text{and} \quad k_- \simeq \frac{qa\rho_b}{2|\sigma_s|}\Gamma^2 \ll k_+. \quad (33)$$

The first equality shows that in the dielectric repulsion GCE regime, the average counterion concentration in the pore, $\langle \rho_+ \rangle = k_+ \rho_b$, is independent of ρ_b and depends only on the pore radius a and the surface charge σ_s . Hence, we are in a regime where dielectric repulsion plays no role in determining the average counterion concentration, which is solely determined by the global electroneutrality in the pore, but excludes coions.

We plot in Fig. 8 the partition coefficient of ions k_{\pm} and the Donnan potential ϕ_0 against the reservoir concentration ρ_b for $\epsilon_m = 2$, $a = 0.84$ nm and a weak surface charge, $|\sigma_s| = 5.4 \times 10^{-4}$ nm $^{-2}$. One observes that at high bulk concentrations, k_+ and k_- decrease when ρ_b decreases, as in the neutral case [and indeed $\phi_0 \approx 0$ since $q\Gamma \gg \gamma$ in Eq. (29), the slight difference $k_+ - k_-$ being given by Eq. (32)] down to a characteristic value ρ_b^c where a discontinuous jump towards a *weak ionic-penetration* state takes place. It is interesting to note that the Donnan potential ϕ_0 also exhibits a jump at this point. A first conclusion is the existence of a discontinuous transition for charged pores at low $|\sigma_s|$, with the coexistence value $\rho_b^c(\sigma_s) \lesssim \rho_b^c(\sigma_s = 0)$. If one further decreases the reservoir concentration, k_- evolves towards vanishingly small values while k_+ abruptly changes by rapidly increasing. We thus reach the dielectric repulsion GCE regime, Eq. (33), denoted by the dotted curve. Although the concentration of ions is low, it is not zero (in order to

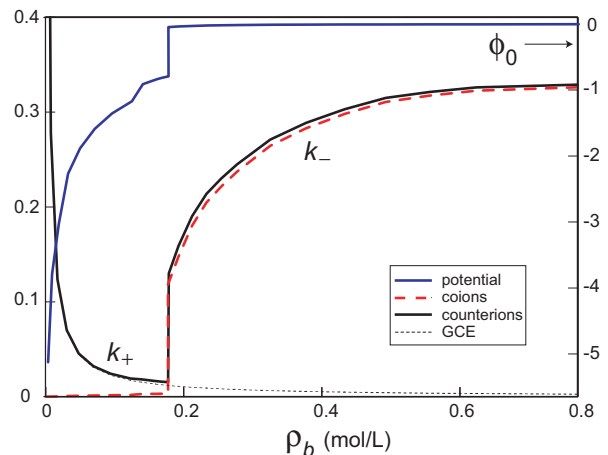
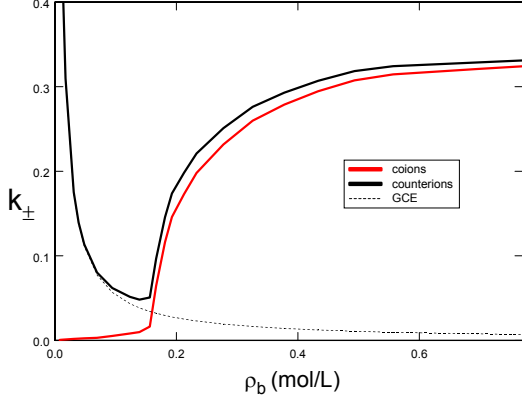


FIG. 8: Partition coefficients of coions and counterions versus the reservoir concentration (above) and the effective Donnan potential (below) for $\epsilon_m = 2$, $\epsilon_w = 78$, $a = 0.84$ nm and $|\sigma_s| = 5.4 \times 10^{-4}$ nm $^{-2}$. The dotted line in the top plot denotes the GCE regime Eq. (33).

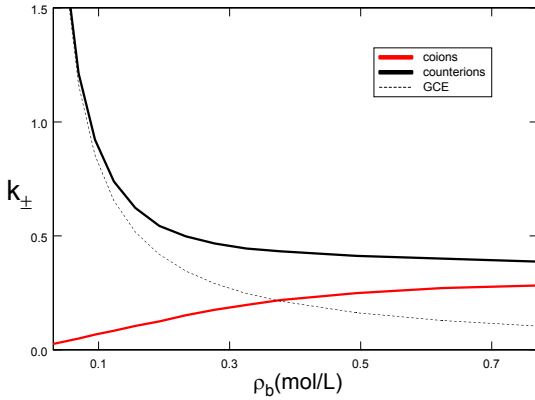
fulfill electroneutrality) and the vapor phase is thus now a *weak ionic-penetration* phase. In this regime, ϕ_0 decreases abruptly since the dielectric exclusion dominates and thus $q\Gamma \ll \gamma$ in Eq. (29).

Figure 9a shows the partition coefficients for a slightly stronger surface charge density $|\sigma_s| = 1.35 \times 10^{-3}$ nm $^{-2}$. In this case, the discontinuous jump disappears and the transition becomes continuous. Hence a large enough fixed surface charge density destroys the first-order phase transition. Figure 9b shows the partition coefficients for a higher surface charge $|\sigma_s| = 2 \times 10^{-2}$ nm $^{-2}$. In this case, not only the discontinuous phase transition, but also the turning point characterizing the abrupt change in the behaviour of k_+ disappears. In other words, above a characteristic surface charge and at low concentrations, the dielectric repulsion GCE regime sets in and the counterion penetration into the pore is solely determined by the global electroneutrality Eq. (33).

In the previous section, we emphasized that the first-order nature of the transition is associated with the variations of δv_0 with κ_v which influences both the DH correlations (which favors the V phase) and the entropy correction (which favors the L phase). The absence of a first-order phase transition when increasing σ_s beyond a characteristic value is due to the decrease of the surface tension associated with the decrease of the external potential for counterions in the first term of Eq. (14), which increases the number of counterions in the nanopore. The complete characterization of the phase transition is illustrated in Fig. 10 where is shown the phase diagram for several values of σ_s . The main effect of the surface charge is to reduce the coexistence line and to shift the critical point towards smaller pore sizes and higher reservoir densities. Comparison of Figs. 10 and 6 clearly shows that the increase of the surface charge plays qualitatively the same role as an increase of the membrane dielectric



(a)



(b)

FIG. 9: Partition coefficients of coions and counterions versus the reservoir concentration for $\epsilon_m = 2$, $\epsilon_w = 78$, $a = 0.84$ nm and $|\sigma_s| = 1.35 \times 10^{-3}$ nm $^{-2}$ (above) and $|\sigma_s| = 2 \times 10^{-2}$ nm $^{-2}$ (below). The dotted line in the top plot denotes the GCE regime Eq. (33).

permittivity. It is important to note that the smearing of the discontinuous phase transition takes place over a very narrow surface charge range: within the parameter regime considered in Fig. 10, the transition completely disappears for $|\sigma_s| > 6.0 \times 10^{-3}$ nm $^{-2}$.

It is well known that nature uses the very same mechanism to deal with strong image forces in water-filled ion channels [34]. As it was illustrated in the Section III, a neutral channel is impermeable to ions at low reservoir concentrations. In potassium channels, negatively charged carbonyl oxygens located at the pore surface [35, 36] reduce the potential barrier induced by image interactions and make the channel cation-selective.

B. Charge regulation mechanism

In the previous part, we considered a boundary surface characterized by a fixed and uniform surface charge. In experiments however, the surface charge density is un-

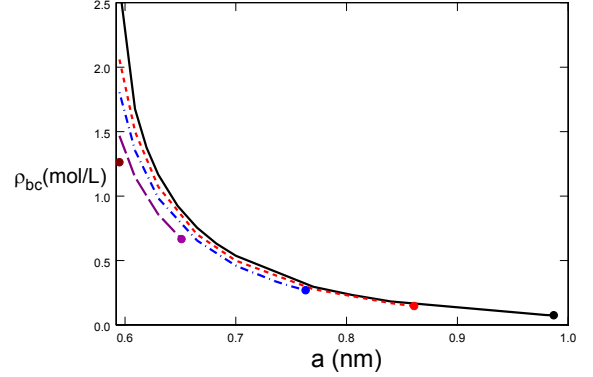
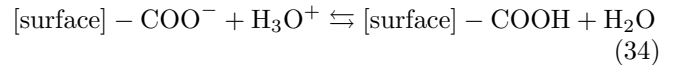


FIG. 10: Phase diagram characterizing the discontinuous phase transition in charged pores for several values of the fixed surface charge. The critical line separates the ion-penetration state (area above the curve) from the ion-exclusion state (area below the curve) and ends at the critical point (dot). $\epsilon_m = 2$ and $\epsilon_w = 78$. From top to bottom, the lines correspond to $|\sigma_s| = 0, 1, 2, 4, 6 \times 10^{-3}$ nm $^{-2}$.

known and cannot be measured easily. Moreover, the pores being designed or self-assembled in carbon membranes, the pH influences σ_s due to some acid groups present at the pore surface. The pH is thus used as a control parameter. In this section, we take into account the fact that, in the presence of water, chemical groups located at the surface may become chemically active, which leads to proton release from the acid groups and to a variable surface charge. Furthermore, the surface groups also interact electrostatically with their own dielectric images and mobile ions in the electrolyte. Hence a surface charging mechanism is introduced in order to investigate the effect of these coupled chemical and electrostatic interactions on ion penetration into cylindrical pores.

The considered charge dissociation mechanism is described by the following chemical equilibrium:

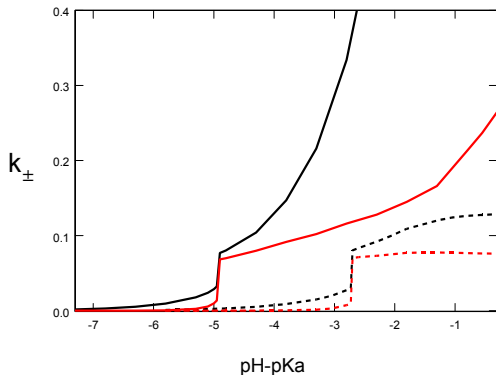


characterized by the equilibrium constant K_a . Writing the law of mass action and the chemical equilibrium of surface hydrogen groups with protons in the bulk, one obtains for the effective surface charge density [37]

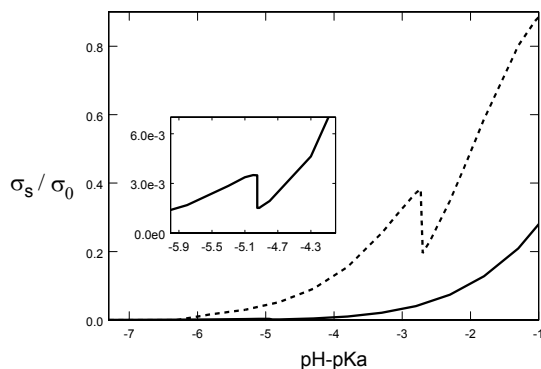
$$\sigma_s = \frac{\sigma_0}{1 + 10^{pK_a - \text{pH}} e^{-w(a-\delta)/2 - \phi_0}}, \quad (35)$$

where $\sigma_0 < 0$ stands for the limiting charge density in the totally dissociated state, $\text{pH} = -\log_{10} \rho_b(\text{H}_3\text{O}^+)$ and δ is a minimum approach distance of these ions to the boundary surface that we estimate in the following at 0.5 Å. In order to satisfy the global electroneutrality in the pore, Eq. (27) should be self-consistently solved with the constant σ_s replaced by Eq. (35).

We consider exclusively the case of trace hydronium ions (H_3O^+) with bulk concentration significantly lower



(a)



(b)

FIG. 11: (a) Partition coefficients of cations (black lines) and anions (red lines) and (b) the reduced surface charge versus $\text{pH}-\text{pKa}$ for $\epsilon_m = 2$, $\epsilon_w = 78$, $\rho_b = 1 \text{ mol/L}$ and $a = 0.617 \text{ nm}$. Solid lines correspond to $|\sigma_0| = 1 \text{ nm}^{-2}$ and dashed lines to $|\sigma_0| = 10^{-2} \text{ nm}^{-2}$. The inset in the bottom plot illustrates the jump in the net surface charge for $|\sigma_0| = 1 \text{ nm}^{-2}$.

than that of the ions in the symmetric electrolyte and thus neglect their presence in the variational grand potential for $2 < \text{pH} < 12$. Fig. 11 illustrates for $\sigma_0 = 1$ and 10 nm^{-2} the ionic partition coefficients (Fig. 11a) and the surface charge (Fig. 11b) versus the acidity of the solvent, $\text{pH} - \text{pKa}$. The low pH regime corresponds to the neutral pore limit, where hydronium ions of high bulk concentration almost totally neutralize the acid groups of the surface and the system is in the weak ionic penetration state. By increasing pH (or decreasing the hydronium concentration in the bulk), the partition coefficient slowly increases until a characteristic value, pH^C , beyond which one crosses the critical line and due to the high surface charge attraction, the system evolves into the ionic penetration state. This transition is illustrated in Fig. 11a by the sudden jump of the coion and counterion partition coefficients, k_{\pm} . The most remarkable prediction of our charge regulation model is that the surface charge density displays a sharp decrease at the

transition point. This behaviour is obviously due to the reduction of the ionic penetration barrier at the transition, which leads to a sudden penetration of hydronium ions in the pore. In other words, the first order transition to the ionic penetration state is accompanied by a surface adsorption (proton binding) transition. These variations of k_{\pm} with pH can explain the fluctuations or switching found in the conductivity of nanopores in PET membranes [17, 38, 39].

V. CONCLUSION

In this article, we develop a variational approach to investigate ion penetration into *cylindrical* nanopores. The variational scheme has already been developed in Ref. [13] and is based on a generalized Onsager-Samaras approximation which assumes a *constant effective screening length*, and a *uniform Donnan potential* enforcing electroneutrality in the pore. These two simplifications to the full variational problem allow us to handle the complicated case of ions confined in a dielectric cylinder.

In the first part of the work, we considered ionic exclusion from a neutral dielectric channel. It is shown that, when the electrolyte concentration in the reservoir or the pore size are decreased down to $\rho_b \simeq 0.1 \text{ mol/L}$ and $a \simeq 1 \text{ nm}$ (see Fig. 6), a first-order phase transition from an ionic-penetration state to an ionic-exclusion one emerges. The physical mechanism behind is a competition between Gibbs adsorption which decreases the surface tension and DH-type attractive correlations strengthened by the presence of the dielectric nanopore wall.

By comparing our predictions to the ones obtained using Yaroshchuk's self-consistent approach [15], it is shown that the latter can over-estimate ion concentration by a factor of 2 to 3. We also propose a continuous description from the slit geometry (thickness d), where no transition but rather a continuous crossover appears [13], to the cylindrical one (diameter $2d$), by describing the case of concentric cylinders (separated by a distance d), thus highlighting the role of dielectric surface curvature.

In the second part, we investigated the effect of a uniform surface charge density on this ionic-exclusion phase transition. When varying bulk concentration, the counterion penetration into the cylindrical channel, induced by the charged surface in order to fulfill the electroneutrality, exhibits a non-monotonic behaviour characterized by two regimes: i) a weak ionic-penetration (or dielectric repulsion GCE) regime, for low reservoir concentrations or small pore sizes, where the decrease of the partition coefficient of coions is even stronger than for a neutral pore, due to dielectric exclusion combined with electrostatic repulsion, and the counterion concentration remains low and is independent of ρ_b . ii) A second regime, reached above a characteristic reservoir concentration, identical to the neutral ionic-penetration phase where repulsive image forces are lower and the electrostatic potential is almost zero. The counter-ion partition coefficient k_{+} in-

creases with the reservoir concentration. Eventually, for very large surface charge density, we again reach the high charge repulsion σ_s GCE regime at the mean-field level, i.e. when dielectric exclusion can be neglected. For very small surface charge densities ($< 2 \times 10^{-3} \text{ nm}^{-2}$), the change between both regimes corresponds to a first-order phase transition. Increasing the surface charge density shrinks the coexistence line and moves the critical point towards smaller pore sizes and higher electrolyte concentrations.

We finally consider the experimental case where the surface charge density varies with the bulk pH by introducing a charge regulation mechanism. The first-order transition survives and qualitatively corresponds to experimental results for conductivity fluctuations measurements in nanopores [17, 39]. Moreover, our charge regulation model predicts an adsorption phase transition of hydronium ions at the pore surface which accompanies the ionic penetration phase transition.

Of course, our model has several limitations. First of all, it neglects ion size, which becomes important for bulk systems at high concentration or strongly charged interfaces where ion concentrations may exceed the close packing value. For a cylindrical pore characterized by strong repulsive image forces where ionic concentrations are always below their bulk value, we expect the ion size effect to play a less important role than in the bulk. However direct correlations between “dressed” ions in the nanopore are neglected and could be taken into account by extending the variational approach adopted in the present work to a second order cumulant expansion. Further investigation will be necessary to estimate the higher order contributions and we expect that it might slightly change the parameter values at coexistence without modifying our qualitative conclusions.

Our present model also neglects ionic polarizability and treats the water solvent as a dielectric continuum of the same polarizability as in the bulk. We are currently working on the generalization of our model to include the polarizability of charged ions, which should yield a more complete picture of the behaviour of large anions in confined geometries. The application of the present model to membrane nanofiltration with practical applications and direct comparison with experiments will be presented in a future work.

Acknowledgments

This work was supported in part by the French ANR (project SIMONANOMEM No. ANR-07-NANO-055).

Appendix A: Green’s function in cylindrical coordinates : single cylinder

In this appendix, we derive the Green’s function $v_0(\mathbf{r}, \mathbf{r}')$ in the presence of a cylindrical dielectric in-

terface of infinite length and radius a . The system is characterized by an electric discontinuity defined by $\epsilon(r) = \epsilon_{<} \Theta(a - r) + \epsilon_{>} \Theta(r - a)$ and a Debye constant $\kappa(r) = \kappa_{<} \Theta(a - r) + \kappa_{>} \Theta(r - a)$, where r denotes the radial distance and \gtrless means $r \gtrless a$. We solve the Debye-Hückel equation

$$[-\nabla(\epsilon(r)\nabla) + \epsilon(r)\kappa^2(r)] v_0(\mathbf{r}, \mathbf{r}') = \beta e^2 \delta(\mathbf{r} - \mathbf{r}') \quad (\text{A1})$$

by exploiting the cylindrical symmetry of the system, i.e. $v_0(\mathbf{r}, \mathbf{r}') = v_0(z - z', \theta - \theta', r, r')$, where θ stands for the azimuthal angle. To this end, we expand $v_0(\mathbf{r}, \mathbf{r}')$ in Fourier space

$$v_0(\mathbf{r}, \mathbf{r}') = \sum_{m=-\infty}^{+\infty} e^{im(\theta-\theta')} \int_{-\infty}^{+\infty} \frac{dk}{4\pi^2} e^{ik(z-z')} \tilde{v}_0(r, r'; m, k). \quad (\text{A2})$$

By injecting this expansion into Eq. (A1) and using

$$\begin{aligned} \delta(\mathbf{r} - \mathbf{r}') &= \frac{1}{r} \delta(r - r') \delta(z - z') \delta(\theta - \theta') \\ \delta(z - z') &= \frac{1}{2\pi} \int_{-\infty}^{\infty} dk e^{ik(z-z')} \\ \delta(\theta - \theta') &= \frac{1}{2\pi} \sum_{m=-\infty}^{+\infty} e^{im(\theta-\theta')}, \end{aligned} \quad (\text{A3})$$

Eq. (A1) reduces to

$$\frac{\partial^2 \tilde{v}_0}{\partial r^2} + \frac{1}{r} \frac{\partial \tilde{v}_0}{\partial r} - \left[\chi_{\gtrless}^2 + \frac{m^2}{r^2} \right] \tilde{v}_0 = -\frac{4\pi\ell_{\gtrless}}{r} \delta(r - r'), \quad (\text{A4})$$

where we have defined $\chi_{\gtrless}^2 = k^2 + \kappa_{\gtrless}^2$ and $\ell_{\gtrless} = \beta e^2 / (4\pi\epsilon_{\gtrless})$. The homogeneous solutions of Eq. (A4) are the modified Bessel functions, $\tilde{v}_0(r, r'; m, k) = A(r') I_m(\chi r) + B(r') K_m(\chi r)$. By taking into account the finiteness of the Green’s function on the cylinder axis $r = 0$ and at infinity $r \rightarrow \infty$ together with the continuity conditions

$$\tilde{v}_0^>(r = a) = \tilde{v}_0^<(r = a) \quad (\text{A5})$$

$$\epsilon_m \frac{\partial \tilde{v}_0^>}{\partial r} \Big|_{r=a} = \epsilon_w \frac{\partial \tilde{v}_0^<}{\partial r} \Big|_{r=a} \quad (\text{A6})$$

$$\frac{\partial \tilde{v}_0^>}{\partial r} \Big|_{r=r'} = \frac{\partial \tilde{v}_0^<}{\partial r} \Big|_{r=r'} - \frac{4\pi\ell_B}{r'}, \quad (\text{A7})$$

one obtains the solution of Eq. (A1) in the form

$$v_0^{\gtrless}(\mathbf{r}, \mathbf{r}') = \ell_{\gtrless} \frac{e^{-\kappa_{\gtrless} |\mathbf{r} - \mathbf{r}'|}}{|\mathbf{r} - \mathbf{r}'|} + \delta v_0^{\gtrless}(\mathbf{r}, \mathbf{r}'). \quad (\text{A8})$$

The first term in the rhs is the usual DH potential in the bulk and the second term, which incorporates the dielectric discontinuity at the interface, reads for $r' < r < a$

$$\delta v_0^<(\mathbf{r}, \mathbf{r}') = \frac{4\ell_{<}}{\pi} \sum'_{m \geq 0} \cos[m(\theta - \theta')] \int_0^\infty dk \cos[k(z - z')] F_m(k; \kappa_{<}, \kappa_{>}) I_m(\kappa_{<} r) I_m(\kappa_{<} r') \quad (\text{A9})$$

$$F_m(k; \kappa_{<}, \kappa_{>}) = \frac{\epsilon_{<} \kappa_{<} K_m(\kappa_{>} a) K'_m(\kappa_{<} a) - \epsilon_{>} \kappa_{>} K_m(\kappa_{<} a) K'_m(\kappa_{>} a)}{\epsilon_{>} \kappa_{>} I_m(\kappa_{<} a) K'_m(\kappa_{>} a) - \epsilon_{<} \kappa_{<} K_m(\kappa_{>} a) I'_m(\kappa_{<} a)}. \quad (\text{A10})$$

and the prime on the summation sign means that the term $m = 0$ must be multiplied by 1/2. Let us note that in the mid-point approximation ($r = 0$), the potential reduces to

$$\delta v_0^<(z = 0) = \frac{4\ell_{<}}{\pi} \int_0^\infty dk \frac{\epsilon_{<} \kappa_{<} K_0(\kappa_{>} a) K_1(\kappa_{<} a) - \epsilon_{>} \kappa_{>} K_0(\kappa_{<} a) K_1(\kappa_{>} a)}{\epsilon_{<} \kappa_{<} K_0(\kappa_{>} a) I_1(\kappa_{<} a) + \epsilon_{>} \kappa_{>} I_0(\kappa_{<} a) K_1(\kappa_{>} a)}. \quad (\text{A11})$$

If the source is located outside the cylinder, one obtains in the region $a < r < r'$

$$\delta v_0^>(\mathbf{r}, \mathbf{r}') = \frac{4\ell_{>}}{\pi} \sum'_{m \geq 0} \cos[m(\theta - \theta')] \int_0^\infty dk \cos[k(z - z')] G_m(k; \kappa_{<}, \kappa_{>}) K_m(\kappa_{>} r) K_m(\kappa_{>} r') \quad (\text{A12})$$

$$G_m(k; \kappa_{<}, \kappa_{>}) = \frac{\epsilon_{>} \kappa_{>} I_m(\kappa_{<} a) I'_m(\kappa_{>} a) - \epsilon_{<} \kappa_{<} I_m(\kappa_{>} a) I'_m(\kappa_{<} a)}{\epsilon_{<} \kappa_{<} K_m(\kappa_{>} a) I'_m(\kappa_{<} a) - \epsilon_{>} \kappa_{>} I_m(\kappa_{<} a) K'_m(\kappa_{>} a)}. \quad (\text{A13})$$

We also report the following coefficients introduced in Eq. (A15)

$$\begin{aligned} J_0(k; \kappa) &= I_0^2(\kappa a) - I_1^2(\kappa a), \\ J_m(k; \kappa) &= I_m^2(\kappa a) - I_{m+1}(\kappa a) I_{m-1}(\kappa a) \quad \text{for } m > 0. \end{aligned} \quad (\text{A14})$$

Finally, in the calculation of the variational grand potential Eq. (14), we perform analytically the integral over the radial distance $r = |\mathbf{r}|$ for the dielectric part which depends on δv_0 , which simplifies to

$$\frac{\Omega_d}{V_p} = \frac{\kappa_v^2}{2\pi^2} \sum'_{m \geq 0} \int_0^1 d\xi \int_0^\infty dk \left[F_m(k; \kappa_v \sqrt{\xi}) J_m(k; \kappa_v \sqrt{\xi}) - F_m(k; \kappa_v) J_m(k; \kappa_v) \right]. \quad (\text{A15})$$

Appendix B: Green's function in cylindrical coordinates : concentric cylinders

We report in this appendix the Green's function solution of Eq. (A4), for concentric cylinders of radius a_1 and a_2 with $a_1 < a_2$. We briefly explain in the end the computation of the variational free energy for this more complicated case. The system is characterized by a dielectric discontinuity defined by $\epsilon(r) = \epsilon_m \Theta(a_1 - r) + \epsilon_w \Theta(r - a_1) \Theta(a_2 - r) + \epsilon_m \Theta(r - a_2)$ and a Debye constant $\kappa(r) = \kappa_v \Theta(r - a_1) \Theta(a_2 - r)$ (we consider only the case of ions confined between the two cylinders). The solution of Eq. (A4) satisfying the boundary conditions

$$\tilde{v}_0^>(r = a_1) = \tilde{v}_0^<(r = a_1) \quad (\text{B1})$$

$$\tilde{v}_0^>(r = a_2) = \tilde{v}_0^<(r = a_2) \quad (\text{B2})$$

$$\epsilon_w \frac{\partial \tilde{v}_0^>}{\partial r} \Big|_{r=a_1} = \epsilon_m \frac{\partial \tilde{v}_0^<}{\partial r} \Big|_{r=a_1} \quad (\text{B3})$$

$$\epsilon_m \frac{\partial \tilde{v}_0^>}{\partial r} \Big|_{r=a_2} = \epsilon_w \frac{\partial \tilde{v}_0^<}{\partial r} \Big|_{r=a_2} \quad (\text{B4})$$

$$\frac{\partial \tilde{v}_0^>}{\partial r} \Big|_{r=r'} = \frac{\partial \tilde{v}_0^<}{\partial r} \Big|_{r=r'} - \frac{4\pi\ell_B}{r'} \quad (\text{B5})$$

is given by

$$v_0(\mathbf{r}, \mathbf{r}') = \ell_B \frac{e^{-\kappa_v |\mathbf{r} - \mathbf{r}'|}}{|\mathbf{r} - \mathbf{r}'|} + \delta v_0(\mathbf{r}, \mathbf{r}') \quad (\text{B6})$$

with

$$\begin{aligned} \delta v_0(\mathbf{r}, \mathbf{r}') &= \frac{4\ell_B}{\pi} \sum_{m \geq 0}^l \cos[m(\theta - \theta')] \int_0^\infty dk \cos[k(z - z')] \{A_m(k; \kappa_v) I_m(\varkappa_v r) I_m(\varkappa_v r') \\ &+ B_m(k; \kappa_v) K_m(\varkappa_v r) K_m(\varkappa_v r') + C_m(k; \kappa_v) [I_m(\varkappa_v r) K_m(\varkappa_v r') + I_m(\varkappa_v r') K_m(\varkappa_v r)]\} \end{aligned} \quad (\text{B7})$$

where we have defined

$$\begin{aligned} A_m(k; \kappa_v) &= \frac{a_m(k; \kappa_v) c_m(k; \kappa_v)}{a_m(k; \kappa_v) b_m(k; \kappa_v) - c_m(k; \kappa_v) d_m(k; \kappa_v)} \\ B_m(k; \kappa_v) &= \frac{d_m(k; \kappa_v) b_m(k; \kappa_v)}{a_m(k; \kappa_v) b_m(k; \kappa_v) - c_m(k; \kappa_v) d_m(k; \kappa_v)} \\ C_m(k; \kappa_v) &= \frac{c_m(k; \kappa_v) d_m(k; \kappa_v)}{a_m(k; \kappa_v) b_m(k; \kappa_v) - c_m(k; \kappa_v) d_m(k; \kappa_v)}, \end{aligned}$$

with the coefficients $a_m(k; \kappa_v)$, $b_m(k; \kappa_v)$ and $c_m(k; \kappa_v)$ defined according to

$$\begin{aligned} a_m(k; \kappa_v) &= \epsilon_m k K_m(\varkappa_v a_1) I'_m(ka_1) - \epsilon_w \varkappa_v I_m(ka_1) K'_m(\varkappa_v a_1) \\ b_m(k; \kappa_v) &= \epsilon_m k I_m(\varkappa_v a_2) K'_m(ka_2) - \epsilon_w \varkappa_v K_m(ka_2) I'_m(\varkappa_v a_2) \\ c_m(k; \kappa_v) &= \epsilon_w \varkappa_v K_m(ka_2) K'_m(\varkappa_v a_2) - \epsilon_m k K_m(ka_2) K'_m(\varkappa_v a_2) \\ d_m(k; \kappa_v) &= \epsilon_w \varkappa_v I_m(ka_1) I'_m(\varkappa_v a_1) - \epsilon_m k I_m(ka_1) I'_m(\varkappa_v a_1), \end{aligned}$$

and $\varkappa_v^2 = \kappa_v^2 + k^2$. The Green's function evaluated at the same point is given by

$$v_0(\mathbf{r}, \mathbf{r}') = v_c^b(0, 0) - \kappa_v \ell_B + \delta v_0(\mathbf{r}, \mathbf{r}') \quad (\text{B8})$$

with

$$\delta v_0(\mathbf{r}, \mathbf{r}) = \frac{4\ell_B}{\pi} \sum_{m \geq 0}^l \int_0^\infty dk \{A_m(k; \kappa_v) I_m(\varkappa_v r)^2 + B_m(k; \kappa_v) K_m(\varkappa_v r)^2 + 2C_m(k; \kappa_v) I_m(\varkappa_v r) K_m(\varkappa_v r)\}. \quad (\text{B9})$$

The DH pressure from an hypothetical bulk solution is now given by

$$p = -\frac{\Omega_v}{L} = -(a_2^2 - a_1^2) \frac{\kappa_v^3}{24} \quad (\text{B10})$$

and the spatial integrations in Eq. (14) are evaluated from $r = a_1$ to $r = a_2$. As in the case with a single

cylindrical pore, the obtained grand-potential energy Ω_v is minimized with respect to κ_v to find the optimal solution to the variational problem.

-
- | | |
|---|--|
| <p>[1] C. Holm, P. Kekicheff, and R. Podgornik, <i>Electrostatic Effects in Soft Matter and Biophysics</i>, Kluwer Academic, Dordrecht (2001).</p> <p>[2] M. Dubois and T. Zemb, <i>Langmuir</i>, 7, 1352 (1991).</p> <p>[3] S. D. Shoemaker and T. K. Vanderlick, <i>Biophys. J.</i>, 83, 2007 (2002).</p> <p>[4] D. J. Bonthuis et al., <i>Phys. Rev. Lett.</i>, 97, 128104 (2006).</p> <p>[5] Verwey EJW, Overbeek JThG, <i>Theory of the stability of lyophobic colloids</i>, Elsevier, Amsterdam (1948).</p> <p>[6] A. Parsegian, <i>Nature</i>, 221, 844 (1969).</p> <p>[7] D. G. Levitt, <i>Biophys. J.</i>, 22, 209 (1978).</p> <p>[8] Y. Levin, <i>Europhys. Lett.</i>, 76, 163 (2006).</p> <p>[9] A. Naji et al., <i>Physica A</i>, 352, 131 (2005).</p> | <p>[10] R.R. Netz and H. Orland, <i>Eur. Phys. J. E</i>, 11, 301 (2003).</p> <p>[11] M.M. Hatlo, R.A. Curtis and L. Lue, <i>J. Chem. Phys.</i>, 128, 164717 (2008)</p> <p>[12] L. Onsager and N. Samaras, <i>J. Chem. Phys.</i> 2, 528 (1934).</p> <p>[13] S. Buyukdagli, M. Manghi, and J. Palmeri, <i>Phys. Rev. E</i> 81, 041601 (2010).</p> <p>[14] A. L. Loeb, <i>J. Colloid. Sci.</i>, 6, 75 (1950).</p> <p>[15] A.E. Yaroshchuk, <i>Adv. Colloid Interf. Sci.</i>, 85, 193 (2000).</p> <p>[16] L. Dresner, <i>Desalination</i>, 15, 39 (1974).</p> <p>[17] A.A. Lev <i>et al.</i>, <i>Proc. R. Soc. Lond. B</i> 252, 187 (1993).</p> <p>[18] B. Jancovici and X. Artru, <i>Mol. Phys.</i>, 49, 487 (1983).</p> |
|---|--|

- [19] S. Buyukdagli, M. Manghi, and J. Palmeri, unpublished.
- [20] D.A. McQuarrie, *Statistical Mechanics* chap.15 (University Science Book, New York, 2000).
- [21] J. Groenewold, *J. Chem. Phys.*, **107**, 9668 (1997).
- [22] T. Arawaka and S. N. Timasheff, *Biochemistry*, **21**, 6545 (1982).
- [23] G. Stell *et al.* *Phys. Rev. Lett.* **37**, 1369 (1976).
- [24] R.R. Singh and K.S. Pitzer, *J. Chem. Phys.* **92**, 6775 (1990).
- [25] M.E. Fisher and Y. Levin, *Phys. Rev. Lett.* **71**, 3826 (1993).
- [26] A.-P. Hynninen and A.Z. Panagiotopoulos, *Mol. Phys.* **106**, 2038 (2008).
- [27] R. Evans, U.M.B. Marconi, P. Tarazona, *J. Chem. Phys.* **84**, 2376 (1986).
- [28] R. Evans, *J. Phys.: Condens. Matter* **2**, 8989 (1990).
- [29] G.S. Heffelfinger, F. van Swol, and K.E. Gubbins, *J. Chem. Phys.* **89**, 5202 (1988).
- [30] B.K. Peterson *et al.*, *J. Chem. Phys.* **88**, 6487 (1988).
- [31] R. Roth and K.M. Kroll, *J. Phys.: Condens. Matter* **18**, 6517 (2006).
- [32] O. Beckstein and M.S.P. Sansom, *Proc. Natl. Acad. Sc. USA* **100**, 7063 (2003).
- [33] L. Onsager, *Chem. Rev.*, **13**, 73 (1933).
- [34] B. Hille, *Ion Channels of Excitable Membranes*, Sinauer Associates, Sunderland, MA (2001).
- [35] J. Zhang, A. Kamenev, B. I. Shklovskii, *Phys. Rev. Lett.* **95**, 148101 (2005).
- [36] J. Zhang, A. Kamenev, and B. I. Shklovskii, *Phys. Rev. E* **73**, 051205 (2006).
- [37] M. Manciu and E. Ruckenstein, *Advances in Colloid and Interface Science*, **105**, 63 (2003).
- [38] S. Buyukdagli, M. Manghi, and J. Palmeri, submitted arXiv:1004.1816 (2010).
- [39] C.A. Pasternak *et al.*, *Colloids Surf. A* **77**, 119 (1993).
- [40] H.J.M. Hijnen and J.A.M. Smit, *Biophys. Chem.* **41**, 101 (1991).